

See discussions, stats, and author profiles for this publication at: <https://www.researchgate.net/publication/316620299>

# What Is the Space of Attenuation Coefficients in Underwater Computer Vision?

Conference Paper · July 2017

DOI: 10.1109/CVPR.2017.68

---

CITATIONS

19

READS

665

6 authors, including:



Derya Akkaynak

Massachusetts Institute of Technology

39 PUBLICATIONS 236 CITATIONS

[SEE PROFILE](#)



Tali Treibitz

University of Haifa

59 PUBLICATIONS 1,065 CITATIONS

[SEE PROFILE](#)



Tom Shlesinger

Tel Aviv University

36 PUBLICATIONS 92 CITATIONS

[SEE PROFILE](#)



Raz Tamir

Tel Aviv University

26 PUBLICATIONS 117 CITATIONS

[SEE PROFILE](#)

Some of the authors of this publication are also working on these related projects:



Microalgae as a source of heat for biodiesel production amateur: development processes and genetic improvement technology on productivity [View project](#)



Red Sea Mesophotic Coral Ecosystems [View project](#)

# What Is the Space of Attenuation Coefficients in Underwater Computer Vision?

Derya Akkaynak<sup>1,2</sup>, Tali Treibitz<sup>1</sup>, Tom Shlesinger<sup>3</sup>, Raz Tamir<sup>2,3</sup>, Yossi Loya<sup>3</sup>, and David Iluz<sup>4</sup>

<sup>1</sup>University of Haifa

<sup>2</sup>Inter-University Institute of Marine Sciences, Eilat

<sup>3</sup>Tel Aviv University

<sup>4</sup>Bar Ilan University

{derya.akkaynak, tomshlez, raztamir6, yosiloya, iluzda}@gmail.com, ttreibitz@univ.haifa.ac.il

## Abstract

*Underwater image reconstruction methods require the knowledge of wideband attenuation coefficients per color channel. Current estimation methods for these coefficients require specialized hardware or multiple images, and none of them leverage the multitude of existing ocean optical measurements as priors. Here, we aim to constrain the set of physically-feasible wideband attenuation coefficients in the ocean by utilizing water attenuation measured worldwide by oceanographers. We calculate the space of valid wideband effective attenuation coefficients in the 3D RGB domain and find that a bound manifold in 3-space sufficiently represents the variation from the clearest to murkiest waters. We validate our model using in situ experiments in two different optical water bodies, the Red Sea and the Mediterranean. Moreover, we show that contradictory to the common image formation model, the coefficients depend on the imaging range and object reflectance, and quantify the errors resulting from ignoring these dependencies.*

## 1. Introduction

The interaction between solar radiation and the upper ocean fuels physical, chemical, and biological processes; and as a result water attenuates light in a wavelength-dependent manner giving the ocean its color and other optical properties [13, 14]. Due to these wavelength-dependent processes, underwater images suffer from reduced contrast and color distortions. As the effect also depends on the distance of the objects, the image degradation is local and cannot be corrected by global operations. To correct the images, both the scene 3D structure and water properties need to be known. While 3D reconstruction is receiving considerable attention, there is almost no research on the range of water properties with respect to computer vision.

Ocean appearance is usually described using color-transmittance dyads like ‘turquoise and clear’ or ‘blue and dark’; but depending on location, season, time of day, and environmental conditions, the ocean color can also be gray,

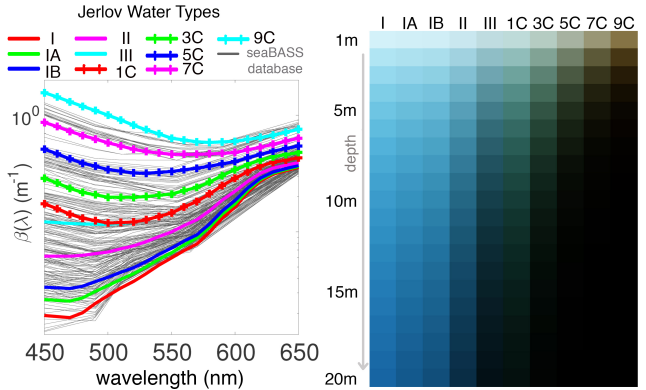
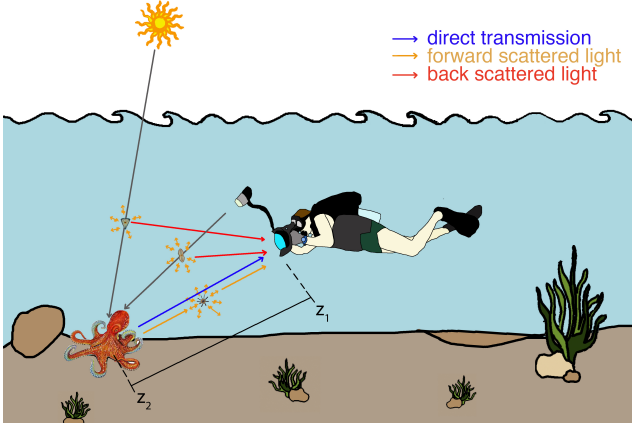


Figure 1. **Water types.** [Left] Based on the attenuation coefficient  $\beta(\lambda)$  measurements from a global expedition between 1947-48 [25], 10 optical classes have come to be known as *Jerlov Water Types* [24]. Types I-III are oceanic waters that range from very clear to slightly murky, and those suffixed with ‘C’ represent coastal waters with increasing turbidity from 1 to 9. Gray lines represent 280 randomly chosen observations from a database [50] that contains more than 60,000 *in situ* measurements taken using modern day equipment between 1989-2015. [Right] RGB simulation of the appearance of a perfect white surface viewed in 1-20m depth in different water types. Note that the common notion that water attenuates red colors faster than blue/green only holds for oceanic water types. We use Jerlov water types to constrain the space of attenuation coefficients in the RGB domain.

brown, black, or even red [6]. Transmittance describes visibility which we might label as ranging from ‘crystal clear’ to ‘murky’, and it is a function of the wavelength-dependent attenuation coefficient of the water body and the distance light has to travel. The attenuation coefficient for the global ocean shows significant spatial and temporal variation as it depends on the concentration of organic and inorganic substances in the water column. How and when their concentrations change depends on complex interactions involving the season, weather, illumination, currents, depth, bathymetry, and other factors [46]. This variation has implications for underwater computer vision where the attenuation information is used for visibility enhancement



**Figure 2. Light propagation underwater.** Object signal is attenuated by the water along the line of sight to the camera (blue arrow). Light that is scattered back to the camera from the water column carries no information about the scene and degrades the image (red arrows). Forward scattered light creates a blurred version of the scene (yellow arrows).

and color restoration algorithms. For example, a visibility enhancement algorithm whose parameters are derived from the clear waters of the Sargasso Sea would perform poorly when applied to photographs from the Baltic Sea, which is characterized by strong light attenuation.

Here, our goal is to leverage the knowledge base from optical oceanography to improve underwater computer vision algorithms. We make the following contributions:

- Using the optical classification of natural water bodies we derive the loci of all physically meaningful RGB attenuation coefficients for underwater imaging. This loci constitutes the valid search space for underwater image reconstruction algorithms, as well as a dictionary for realistic computer-generated imagery and rendering of natural waters.
- Through the derivation of wideband coefficients, we show that they depend on scene properties in addition to water properties, a dependency that is ignored in the currently used image formation model.
- We validate our proposed loci by *in situ* experiments through scuba diving in two different water bodies: the Red Sea (tropical) and the Mediterranean (temperate).

## 2. Related Work

Recent single image reconstruction methods (for haze and underwater) assume wavelength independent attenuation and thus avoid the need to estimate color-dependent attenuation [4, 5, 10, 15, 16, 21, 29, 33, 47]. Some underwater works used fixed coefficients for reconstruction, which only suit specific cases [11].

Other methods used multiple images and recovered channel dependent optical depth (the multiplication of attenuation and distance) [39, 41] or related parameters [48].

The basic estimation method for attenuation coefficients is to acquire an image of a known calibration target at known distances [1, 31, 51], however this requires external hardware and distance measurement. Instead, most methods use multiple images of the same object from several distances, where only their difference has to be known [52], or that are known from a sonar [28] or structure-from-motion [9]. Some of these ignore scattering and therefore can be used only when water is clear [28, 52]. Recently, [44] used backscatter images for calibration. In [8], the grey-world assumption is used, but this does not always hold especially when looking into the water column. In a lab setup [32] used a single image of a light source. None of these methods verified the results to be physically feasible.

Ill-posed or noisy computer vision problems traditionally benefit from constraining the set of solutions. Such a strategy is very common in tasks of estimating wavelength-dependent functions that theoretically have many unknowns (one per each wavelength): for example, color constancy [7, 30], reflectance and illumination estimation [35, 38, 42], or estimating camera response functions [20] or spectral sensitivities [27].

## 3. Light Propagation Underwater

### 3.1. Optical Classification of the World’s Oceans

The first systematic assessment of the optical properties of the global ocean was made by Jerlov and colleagues [24] during the Swedish Deep Sea Expedition of 1947-48 [25]. They measured the downwelling irradiance at various depths, from which they obtained the total attenuation coefficient  $\beta(\lambda)$  (Fig. 1, left). Based on these values, Jerlov categorized the world’s oceans into five oceanic and five coastal classes.

Optical properties of the ocean are governed by the type and density of the particles suspended in the water column. Two independent mechanisms, absorption and scattering, determine the amount of attenuation light will experience as it travels and encounters these particles (Fig. 2). The total attenuation coefficient  $\beta(\lambda)$  is their summed effect [3, 12]. In the open ocean these particles are almost always drifting algae called *phytoplankton* with a well characterized spectral signature, attenuating the longer wavelengths (i.e., red colors) much faster than shorter ones, resulting in an overall bluish appearance. In the coastal oceans, optically active impurities dumped by rivers or from agricultural runoff may dominate, causing short wavelengths to attenuate just as strongly as long ones (Fig. 1, right).

Jerlov’s classification is not all-encompassing for all water bodies in the world; for example, it cannot represent the attenuation in very murky coastal lagoons or extremely turbid lakes such as those reported by [34, 37]. However, it is regarded as a compact representation of global water color

and transmittance [43]. The recent seaBASS database [50] contains over fifty thousand *in situ* water attenuation measurements taken using modern day instruments since 1989. Qualitatively, they all appear within the range of the Jerlov water types. A randomly chosen subset of these data is shown in Fig. 1.

### 3.2. Image Formation Underwater

Fig. 2 depicts the trajectory of light reflected from the skin of an octopus traveling towards the sensor of the diver's camera. The commonly used image formation model for computer vision in scattering media states that in each color channel  $c \in \{R, G, B\}$  the image intensity  $I_c$  at each pixel  $\mathbf{x}$  is composed of two components: attenuated signal and veiling light [22, 40]:

$$I_c(\mathbf{x}) = D_c(\mathbf{x}) + B_c(\mathbf{x}) \quad (1)$$

Directly transmitted light  $D$  carries the object signal, attenuated by the water along the line of sight to the camera (Fig. 2, blue arrow). The backscattering component  $B$ , also called veiling light, carries no information about the scene and therefore degrades most of the color and contrast in the image (Fig. 2, red arrows). Forward scattered light also carries information about the scene, but it loses intensity and structure due to scattering along its trajectory before reaching the sensor (Fig. 2, yellow arrows), creating a blurred version of the scene. Compared to attenuation experienced by the directly transmitted light, that of forward scattered light is negligible, and has been shown to minimally affect image degradation [15, 40, 48]. In this work we focus on attenuation coefficients, and therefore only consider the direct transmission signal.

The transmission is set by the Beer-Lambert law [40]:

$$D(z_2, \lambda) = D(z_1, \lambda)e^{-\int_{z_1}^{z_2} \beta(z', \lambda)dz'} \quad (2)$$

where  $z_1$  and  $z_2$  are the start and end points along the LOS, respectively,  $\lambda$  is wavelength, and  $\beta$  is the attenuation coefficient of the water body. Assuming the water volume is spatially homogeneous ( $\beta(z, \lambda) = \beta(\lambda)$ ) simplifies Eq. 2 :

$$D(z_2, \lambda) = D(z_1, \lambda)e^{-\beta(\lambda)\Delta z}, \quad (3)$$

where  $\Delta z = z_2 - z_1$ .

Now, the apparent color of a surface captured by a sensor with spectral response  $S_c(\lambda)$  at a distance  $z$  is:

$$D_c = \frac{1}{\kappa} \int_{\Lambda} S_c(\lambda) \rho(\lambda) E(\lambda) e^{-\beta(\lambda)z} d\lambda, \quad c = R, G, B \quad (4)$$

where  $\rho(\lambda)$  is the reflectance spectrum of the surface of interest and  $E$  is the illumination irradiance. Here  $\kappa$  is a scaling constant governing image parameters, such as exposure.

Reconstruction algorithms usually aim to recover the unattenuated colors of the original scene, denoted by  $J_c$ :

$$J_c = D_c(z = 0). \quad (5)$$

## 4. Effective Wideband Attenuation

Eq. 4 incorporates the wavelength dependent nature of  $\beta$  in the overall color signal  $D_c$ . When working with wideband cameras, it is common to express attenuation by wideband channels, simplifying Eq. 4 to the following [9, 39]:

$$D_c(z + \Delta z) = D_c(z)e^{-\beta_c \Delta z}, \quad (6)$$

where we term  $\beta_c$  as the *effective wideband attenuation coefficient*. This simplification offers two advantages (at the cost of accuracy, which we discuss shortly). First, it reduces the number of unknowns that need to be estimated for  $\beta$  to three, one for each color channel of an RGB camera. Second, by removing the wavelength dependency, it makes it possible for the term  $e^{-\beta \Delta z}$  to be taken outside of the integration.

When the direct signal and range  $z$  are known or estimated, the unattenuated image signal  $J_c$  can be recovered:

$$\hat{J}_c = D_c e^{\beta_c z}. \quad (7)$$

Following Eq. 6 the wideband attenuation coefficient is defined as

$$\beta_c = \ln \left[ \frac{D_c(z)}{D_c(z + \Delta z)} \right] / \Delta z, \quad (8)$$

i.e., based on Eq. 4, for Eq. 6 to hold, the effective attenuation coefficient  $\beta_c$  has to obey:

$$\beta_c = \ln \left[ \frac{\int S_c(\lambda) \rho(\lambda) E(\lambda) e^{-\beta(\lambda)(z)} d\lambda}{\int S_c(\lambda) \rho(\lambda) E(\lambda) e^{-\beta(\lambda)(z+\Delta z)} d\lambda} \right] / \Delta z. \quad (9)$$

It can be seen that  $\beta_c$  in Eq. 9 depends on  $S_c$ ,  $z$ ,  $\Delta z$ ,  $\rho$  and  $E$ , as opposed to  $\beta(\lambda)$  that is a property of the water. It is clear that the simplifications in the commonly used image formation model results in Eq. 6 not being an analytical result of Eq. 9, and the quality of the approximation also depends on the camera and the imaged scene. Next, we move on to quantify the space that physically feasible  $\beta_c$  can occupy, and then analyze these limitations.

### 4.1. Space of Wideband Attenuation Coefficients

We projected the attenuation coefficients  $\beta(\lambda)$  of the 10 Jerlov water types into the RGB domain using Eq. 9. Fig. 3a shows the  $\beta_c$  values calculated for oceanic (denoted by X's) and coastal water types (filled circles), where the color of each marker describes one of the water types from Fig. 1. We used the spectral response curves of a Nikon D90 camera from the database of [27]. For simplicity, we assumed  $\rho = E = 1$  in Eq. 9 and used  $z_1 = 0$  and  $z_2 = 10m$ . The 10 Jerlov water types are discrete, and we do not expect the attenuation to bounce between them in nature. Instead, we show that for a specific camera and distance the values of  $\beta_c$

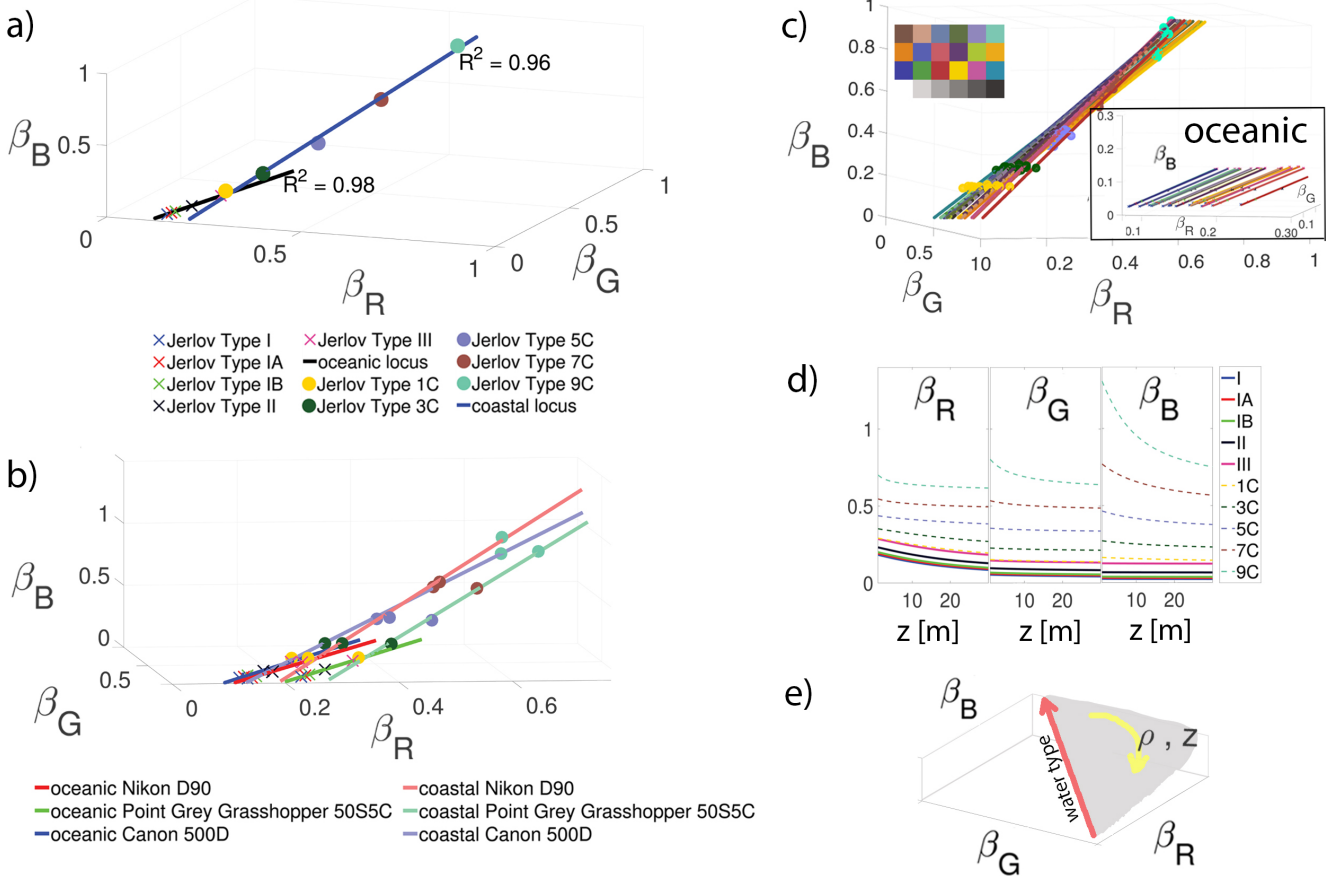


**Figure 3. Space of wideband attenuation coefficients.** a) Based on Jerlov water types, we derived the coordinates of the RGB attenuation coefficients  $\beta_c$  for oceanic (X's) and coastal (filled circles) waters using Eq. 9, which fall on two lines in 3-dimensional space. In all subplots, we used the spectral response of a Nikon D90 camera from [27], and  $z = 10\text{m}$  for modelling. b) Shifting of the  $\beta_c$  locus based on the spectral response of the camera sensor used. c) Shifting of the  $\beta_c$  locus based on radiance, shown here for each of the 24 patches of a Macbeth ColorChecker (inset) under D65 illuminant. d) Sensitivity of  $\beta_c$  to the values of range  $z$  used to calculate it. For oceanic water, larger ranges result in higher attenuation in the red channel, but for very turbid coastal waters the effect is greater in the blue channel. For example, for type I waters  $\beta_R$  is 14% higher at 5 meters than its magnitude at 10 meters, while this is only 2% for water type 9C. Conversely, for type 9C waters in the blue channel  $\beta_B$  is approximately 14% higher at 5 meters than its value at 10 meters, while it remains constant for type I waters. e) For a given sensor, the locus of  $\beta_c$  (shown here for oceanic water) spans the area highlighted in gray, as the range and radiance are varied. In this example, we used the radiance from c) and changed  $z$  from 1 to 30 meters. **Throughout the paper the units of  $\beta_c$  are  $\text{m}^{-1}$ .**

are located along a 1D manifold, containing two lines- one for open water and one for coastal. Attenuation measurements that are between water types are likely to fall along these lines. The rationale behind the linear shape of the locus might be that a main component in attenuation is the absorption of pure water and variations from it stem from different concentrations of several types of organisms and particles in water [2].

The loci (black line for oceanic, blue for coastal waters) were fit using minimum mean square distance in 3-space and are almost perfect linear with  $R^2$  (quality of fit) values very close to 1. This result reduces the potential space of coefficients from the entire  $\mathcal{R}^3$  to a limited manifold.

Based on Eq. 9, an alarming result is that the wideband attenuation coefficients  $\beta_c$  depend on scene reflectance  $\rho$ , ambient light spectrum  $E$ , spectral response of the camera  $S_c$ , and range  $\Delta z$ . This contradicts the standard image formation model (Eq. 6). We now explore how our basic result (Fig. 3a) depends on them.

Fig. 3b shows how coefficients shift due to the response of three different sensors: Nikon D90, Canon 500D and Point Grey Grasshopper, whose spectral sensitivities we adopted from [27]. The inter-camera variation can be potentially standardized by calibrating the camera, e.g., transforming the spectral response into the CIE RGB 10-degree observer space [45], but this requires knowledge of the cam-

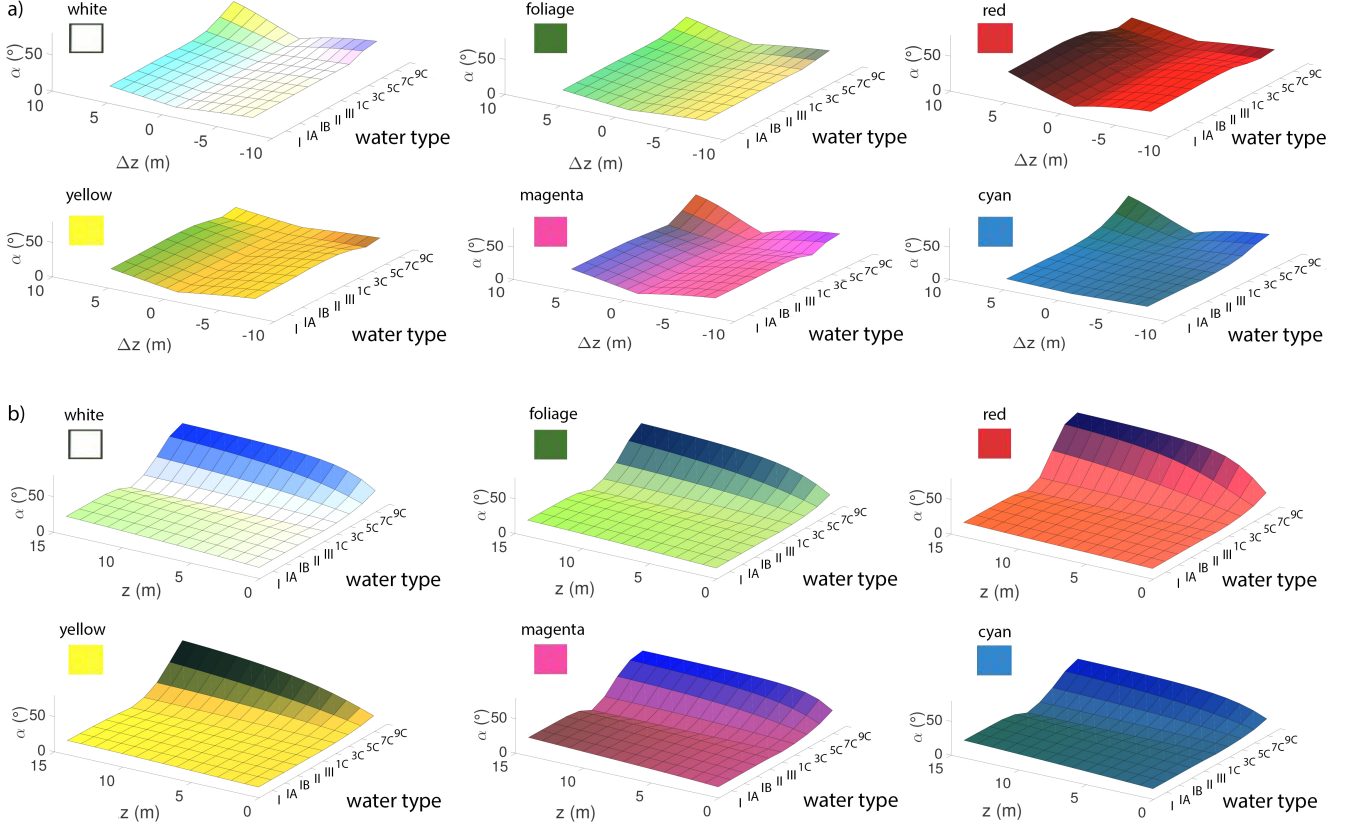


**Figure 4. Visualization of errors when incorrect  $\beta_c$  is used.** We used the white, foliage, red, yellow, magenta and cyan patches of a Macbeth ColorChecker to demonstrate the errors in color correction when a)  $\beta_c$  is calculated using an incorrect range  $z$ , and b) from an incorrect water type. a) We simulated the patches at 7m depth, with ambient light D65 at the sea surface, and calculated the appearance of each patch when corrected by  $\beta_c$  obtained with  $z$  values ranging from 1 – 14m. The z-axis shows the error (Eq. 10) between the unattenuated colors and those obtained by using incorrect  $\beta_c$ . The rest of the colors on each surface show the *distorted* colors resulting from an incorrect  $\beta_c$ . For oceanic waters, colors that contain red are most affected by larger errors in  $z$ . b) We simulated the appearance of the same patches in water type 1C, but corrected with  $\beta_c$  calculated from other water types at depths of 1-15m. In both a) and b), errors are higher for coastal water classes, and for increasing ranges. For visualization purposes, in both a) and b), we normalized the resulting colors for each patch by the maximum value encountered for that patch across all depths and water types.

era spectral sensitivity.

In Fig. 3c, we use radiance (the product of reflectance and illumination) to demonstrate the combined effect on the patches of a Macbeth ColorChecker (X-Rite, Inc.) illuminated under the CIE 65 light. This dependency was also recently observed empirically by [44]. For oceanic waters, the locus simply shifts in 3-space, but for coastal waters which are associated with strong attenuation, the locus changes only very slightly.

In Fig. 3d, we used  $z_1 = 1$  and varied  $z_2$  up to 30 meters to calculate the shift of  $\beta_c$ . The  $z$  dependency is more prominent in water types where the attenuation coefficient changes rapidly within the sensitivity range of one of the color channels, for example, the red range in coastal waters.

Fig. 3e summarizes the space of  $\beta_c$  values for a given camera. Variations in water type, scene radiance, and range

result in the sweeping of a 2D plane of possible  $\beta_c$  values.

#### 4.2. Sensitivity of Reconstruction to Error in Attenuation Coefficients

We showed in the previous section that in practice the effective attenuation coefficients may vary within the same scene because of dependencies on distance and reflectance, as opposed to the common notion (Eq. 6). In this section we examine how much these errors influence color reconstruction. To examine the best-case scenario, we assume backscatter was removed properly, and look only at the error in compensating for attenuation of the direct signal (Eq. 7).

Fig. 4a visualizes errors resulting from ignoring the  $z$  dependency of  $\beta_c$ . We show the reconstructed colors of six Macbeth chart patches, for  $z = 7$ m, using  $\beta_c$  estimated for a different  $z$ , for all water types. We quantify the error be-

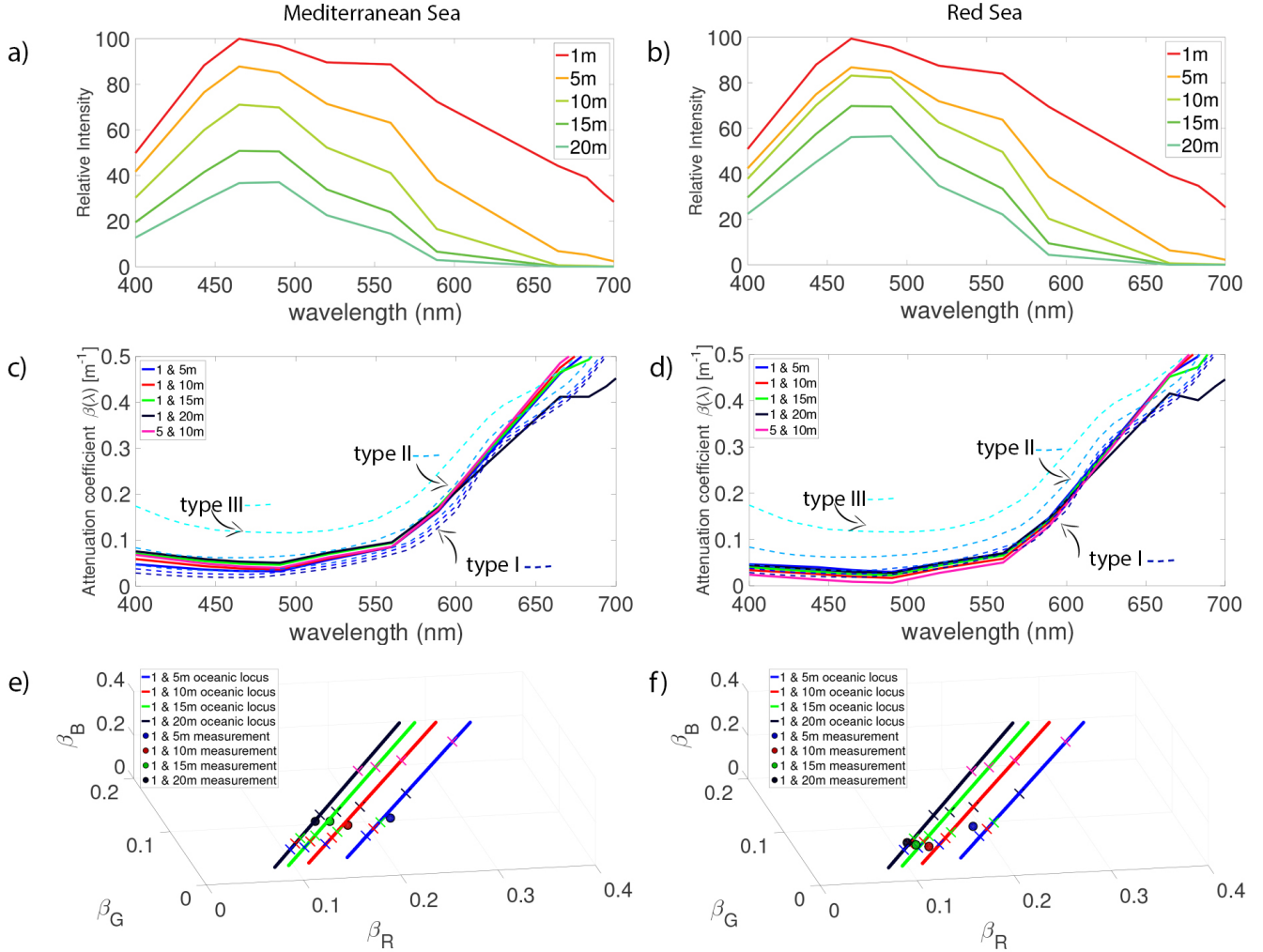


**Figure 5. Validation of our model.** We measured spectral irradiance *in situ* at 1,5,10,15 and 20 meters depth in the Mediterranean Sea (a) and the Red Sea (b). From these irradiance measurements, we calculated the attenuation coefficient  $\beta(\lambda)$  according to Eq. 2. Dashed lines represent Jerlov's water types I-III. The Mediterranean is most similar to Jerlov's oceanic type II characterization (c), and the Red Sea is clearer, closer to a type I (d). The attenuation coefficient we measured *in situ* falls on the oceanic water locus derived based on Jerlov's water types for both the Mediterranean Sea and the Red Sea. (e) and the tropical sea (f) Here, we adjusted the locus of  $\beta_c$  for the ranges  $z_1$  and  $z_2$  we used to calculate the attenuation.

tween the unattenuated color  $J$  and the one reconstructed using Eq. 5 with incorrect  $\beta_c$ ,  $\hat{J}$  in the RGB space using:

$$\cos \alpha = J \cdot \hat{J} / (|J| \cdot |\hat{J}|) , \quad (10)$$

where the angle  $\alpha$  yields dissimilarity between them. In general, the hue of the reconstructed colors shifts whether  $\beta_c$  was estimated using longer or shorter ranges, and the larger the  $\Delta z$ , the more prominent this effect gets. Water type also affects this shift; for example, the white patch can appear purplish when imaged in water type 9C if corrected with  $\beta_c$  estimated from shorter depths, or yellowish if corrected with  $\beta_c$  estimated from longer ranges.

In Fig. 4b, we simulated the same Macbeth chart patches in water type 1C, and visualize the errors resulting from

$\beta_c$  estimated from other water types, at depths of 1-15m. While the errors remain small for water types I-III at each depth, they increase for all coastal water types, and as in the previous case, cause hue shifts.

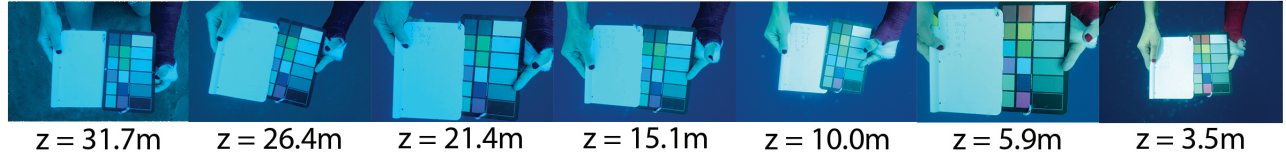
As we showed earlier,  $\beta_c$  also depends on other parameters. In general, the error  $e_J$  in the recovered image  $J$  due to the error  $e_\beta$  in estimating  $\beta$  can be quantified as:

$$e_J = \frac{\delta J}{\delta \beta} e_\beta . \quad (11)$$

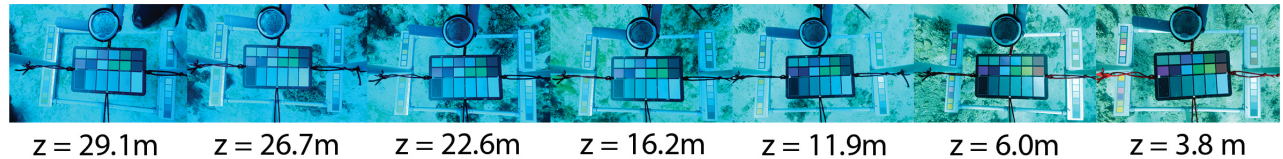
Differentiating Eq. 7 yields  $\frac{\delta J}{\delta \beta_c} = z J_c$  and substituting this in Eq. 11 yields

$$\frac{e_J}{J} = z e_\beta . \quad (12)$$

a) Experiments in the Mediterranean



b) Experiments in the Red Sea



c) Locus validation

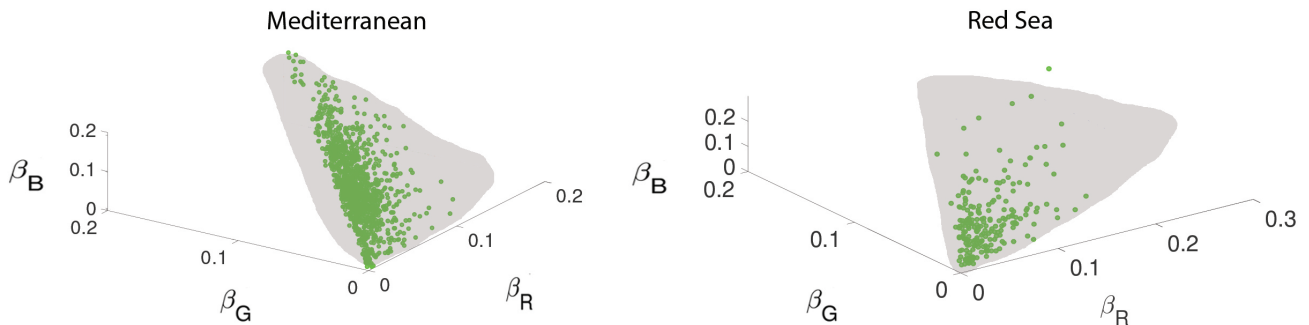


Figure 6. **Experiments validating our model.** a,b) Synchronized with our *in situ* light measurements in Fig. 5, we went SCUBA diving to 31 meters and photographed a color calibration target in roughly 5 meter intervals. This was done in two optically different water bodies, Mediterranean (type II), and the Red Sea (type I). c) From these images we calculated  $\beta_c$  using Eq. 8. Each green circle represents  $\beta_c$  calculated between corresponding patches photographed at various depth combinations. These are compared to the loci from our theoretical derivation (Eq. 9), depicted as a gray plane. The loci was derived using the measured *in situ*  $\beta(\lambda)$  (Fig. 5), Nikon camera sensitivity, with varying  $z$ ,  $\rho$  and  $E$ . The observed  $\beta_c$  fall within the loci predicted by our model (gray planes).

Thus, the relative reconstruction error linearly increases with the object distance and the error in  $\beta_c$ .

## 5. Real-World Experiments

### 5.1. Attenuation as a Function of Wavelength

We conducted *in situ* experiments underwater in the Red Sea (tropical water body) and the Mediterranean (temperate water body) to validate our analysis. We deployed a profiling reflectance radiometer from a boat (PRR800, Biospherical Instruments) which measured downwelling irradiance underwater from the surface to 20 meters depth (Fig. 5a,b), sampling 19 channels between 300–900 nm. The radiometer was deployed at late morning using the free-fall technique [49] to avoid shade or reflectance from the boat and to maintain the light sensor in a vertical orientation. The data was analyzed using the PROFILER software from the manufacturer. We then calculated the attenuation coefficient  $\beta$  (Fig. 5c,d) according to Eq. 2. The measured attenuation falls within oceanic water types in both cases: our Mediterranean dive site was type II, and Red Sea, type I.

Next, we used Eq. 9 to calculate  $\beta_c$  using the measured attenuation, in different ranges. Fig. 5e,f shows that our *in situ* attenuation measurements (filled circles) in the Mediterranean fall between Jerlov's water types IB and II on the derived line, which agrees with previous characterizations of this water body [26]. The attenuation measurements for the Red Sea fall on the space around water type I, which generally describes clear to slightly turbid tropical waters.

### 5.2. Validation of Effective Wideband Coefficients

Synchronized with our *in situ* light measurements, we went SCUBA diving and photographed a color calibration target (DGK Color Tools) at depths ranging from 30 meters to the surface, in roughly 5 meter intervals (Fig. 6). We used a Nikon D90 camera equipped with a Nikkor 12-24 mm lens, in an Ikelite housing. All photos were taken at fixed magnification, aperture and ISO, with only the shutter speed varying, and no more than 5 cm away from the color chart to avoid backscatter. We standardized exposure across all images by compensating for shutter speed. Images acquired

are shown in Fig. 6a,b for the Mediterranean and the Red Sea, respectively. Then, using Eq. 8 we calculated  $\beta_c$  from the images for each of the color patches.

Fig. 6c depicts the calculated  $\beta_c$  values from the images, overlaid on the plane of physically-feasible values calculated using Eq. 9. We used the Nikon camera, the  $\beta(\lambda)$  measured *in situ* and varied  $z, \rho$  and  $E$ . For the Mediterranean, we derived the locus for water type II, and water type I for the Red Sea. The resulting  $\beta_c$  values calculated from the images within the plane that stems from Eq. 9, validating our analysis.

Our photographs taken *in situ* mostly reflect the behavior of  $\beta_c$  in our simulations, but with some shifts. These differences are more pronounced in the dives at the temperate water site, in which the color chart was held steady by a diver suspended in blue water, where in the tropical dive site, it was possible to place the chart on the seafloor and measure depth with greater accuracy.

## 6. Application to Other Scattering Media

In this section, we extend our methodology to milk and red wine, two commonly used participating media in computer vision and graphics. The optically important components in milk that affect its appearance are fat and protein molecules. Authors in [17, 18] developed an appearance model for milk based on the Lorenz-Mie scattering theory, modelling the wavelength-dependent of attenuation coefficient  $\beta(\lambda)$  for a given fat weight and protein content. Using a constant protein content and varying fat content from 0.2 to 10 %, we derived the space of  $\beta_c$  coefficients for milk using a range of 1 mm (Fig. 7, X's). Others have estimated the RGB attenuation coefficients of milk using different methodologies [19, 23, 32], and these data show good agreement with the line we have derived. Similarly,  $\beta(\lambda)$  for different kinds of red wine are provided in [36]. In Fig. 7b, we used four different kinds of red wine (X's) to derive the line that represents the valid space of  $\beta_c$ , and compared these to previously published measurements of extinction coefficients in red and rose wine [19, 32].

## 7. Discussion

We showed that the range of wideband attenuation coefficients in the ocean is limited. Moreover, we showed that the common naïve transition from wavelength dependent attenuation  $\beta(\lambda)$  to wideband attenuation  $\beta_c$  is not as straightforward as was done until now. The wideband coefficients become sensitive to the object range and original color. This invalidates the commonly used image formation model to some extent and we analyzed the expected errors from this discrepancy. We validated our model with *in situ* experiments in two types of water.

This analysis triggers many questions and research di-

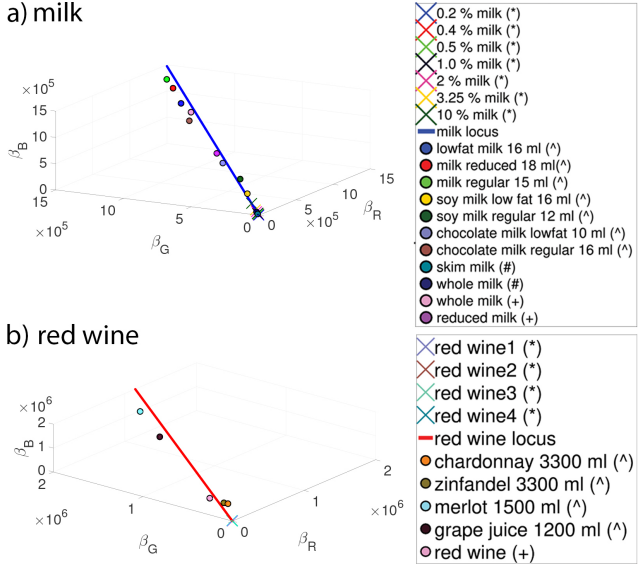


**Figure 7. Application to scattering media other than ocean water.** a) We used  $\beta(\lambda)$  for milk derived as a function of fat and protein content (X's) by [17], and show that the corresponding locus is also linear. Filled circles represent previously published attenuation (extinction) coefficients estimated from photos using dilution (marked with ^ [32]), models of subsurface light transport (marked with # [23]), and Lorenz-Mie theory (marked with + [18]). Note that here we derived the locus using the spectral response of a Nikon D90 camera, and the sensors used in these publications were different. b) Locus of RGB attenuation coefficients for red wine, using  $\beta(\lambda)$  curves given in [36]. Filled dots represent previously published coefficients for various types of red wine. Those marked with ^ were obtained from [32], and + represents a data point from [19].

rections. In the future we are planning to develop methods that take into account the dependencies we showed. For example, use a pre-measured range map and reconstruct the image using distance-dependent coefficients. In addition, using our analysis we can infer the water type out of the coefficients, and consequently bio-optical properties, if the camera's sensitivity is known. Relating the ocean's bio-optical properties to the RGB domain will enable the use of RGB cameras in two new functions: for reliable ecological monitoring (e.g., plankton biomass estimation, harmful algal blooms, floods, oil spills, etc.); and for validation of remotely sensed datasets of ocean color.

## Acknowledgements

This work was supported by the The Leona M. and Harry B. Helmsley Charitable Trust, the Maurice Hatter Foundation, and Ministry of Science, Technology and Space grant #3 – 12487, the Technion Ollendorff Minerva Center for Vision and Image Sciences, the University of Haifa institutional postdoctoral program and the Inter-University Institute of Marine Sciences in Eilat postdoctoral fellowship.

## References

- [1] D. Akkaynak, T. Treibitz, B. Xiao, U. A. Gürkan, J. J. Allen, U. Demirci, and R. T. Hanlon. Use of commercial off-the-shelf digital cameras for scientific data acquisition and scene-specific color calibration. *JOSA A*, 31(2):312–321, 2014.
- [2] R. Austin and T. Petzold. Spectral dependence of the diffuse attenuation coefficient of light in ocean waters. *Optical Engineering*, 25(3):253471–253471, 1986.
- [3] M. Babin, D. Stramski, G. M. Ferrari, H. Claustre, A. Bricaud, G. Obolensky, and N. Hoepffner. Variations in the light absorption coefficients of phytoplankton, non-algal particles, and dissolved organic matter in coastal waters around europe. *J. Geophysical Research: Oceans*, 108(C7), 2003.
- [4] D. Berman, T. Treibitz, and S. Avidan. Non-local image dehazing. In *Proc. IEEE CVPR*, 2016.
- [5] D. Berman, T. Treibitz, and S. Avidan. Air-light estimation using haze-lines. In *Proc. IEEE ICCP*, 2017.
- [6] D. Blondeau-Patissier, J. F. Gower, A. G. Dekker, S. R. Phinn, and V. E. Brando. A review of ocean color remote sensing methods and statistical techniques for the detection, mapping and analysis of phytoplankton blooms in coastal and open oceans. *Progress in oceanography*, 123:123–144, 2014.
- [7] D. H. Brainard and W. T. Freeman. Bayesian color constancy. *JOSA A*, 14(7):1393–1411, 1997.
- [8] M. Bryson, M. Johnson-Roberson, O. Pizarro, and S. B. Williams. Colour-consistent structure-from-motion models using underwater imagery. In *Robotics: Science and Systems*, 2012.
- [9] M. Bryson, M. Johnson-Roberson, O. Pizarro, and S. B. Williams. True color correction of autonomous underwater vehicle imagery. *J. of Field Robotics*, 2015.
- [10] N. Carlevaris-Bianco, A. Mohan, and R. M. Eustice. Initial results in underwater single image dehazing. In *Proc. IEEE/MTS Oceans*, 2010.
- [11] J. Y. Chiang and Y.-C. Chen. Underwater image enhancement by wavelength compensation and dehazing. *IEEE Trans. Image Processing*, 21(4):1756–1769, 2012.
- [12] T. Dickey and P. Falkowski. Solar energy and its biological-physical interactions in the sea. *The sea*, 12:401–440, 2002.
- [13] T. Dickey, M. Lewis, and G. Chang. Optical oceanography: recent advances and future directions using global remote sensing and in situ observations. *Reviews of Geophysics*, 44(1), 2006.
- [14] H. M. Dierssen and K. Randolph. Remote sensing of ocean color. In *Earth System Monitoring*, pages 439–472. Springer, 2013.
- [15] P. Drews, E. Nascimento, F. Moraes, S. Botelho, and M. Campos. Transmission estimation in underwater single images. In *Proc. IEEE ICCV Underwater Vision Workshop*, pages 825–830, 2013.
- [16] R. Fattal. Dehazing using color-lines. *ACM Trans. on Graphics (TOG)*, 34(1):13, 2014.
- [17] J. R. Frisvad. Light, matter, and geometry. 2008.
- [18] J. R. Frisvad, N. J. Christensen, and H. W. Jensen. Computing the scattering properties of participating media using lorenz-mie theory. *ACM Trans. on Graphics (TOG)*, 26(3):60, 2007.
- [19] I. Gkioulekas, S. Zhao, K. Bala, T. Zickler, and A. Levin. Inverse volume rendering with material dictionaries. *ACM Trans. on Graphics (TOG)*, 32(6):162, 2013.
- [20] M. D. Grossberg and S. K. Nayar. Modeling the space of camera response functions. *Trans. IEEE PAMI*, 26(10):1272–1282, 2004.
- [21] K. He, J. Sun, and X. Tang. Single image haze removal using dark channel prior. In *Proc. IEEE CVPR*, 2009.
- [22] J. S. Jaffe. Computer modeling and the design of optimal underwater imaging systems. *IEEE J. Oceanic Eng.*, 15(2):101–111, 1990.
- [23] H. W. Jensen, S. R. Marschner, M. Levoy, and P. Hanrahan. A practical model for subsurface light transport. In *Proc. Conf. Computer graphics and interactive techniques*, pages 511–518, 2001.
- [24] N. Jerlov. *Irradiance Optical Classification*. Elsevier, 1968.
- [25] N. Jerlov and A. (Schooner). *Optical Studies of Ocean Waters*. Reports of the Swedish Deep-Sea Expedition, 1947–1948 ; v. 3: Physics and chemistry. Elanders boktr, 1957.
- [26] N. G. Jerlov. *Marine optics*, volume 14. Elsevier, 1976.
- [27] J. Jiang, D. Liu, J. Gu, and S. Susstrunk. What is the space of spectral sensitivity functions for digital color cameras? In *IEEE Workshop Applications of Computer Vision (WACV)*, pages 168–179, 2013.
- [28] J. W. Kaeli, H. Singh, C. Murphy, and C. Kunz. Improving color correction for underwater image surveys. In *Proc. IEEE/MTS Oceans*, pages 805–810, 2011.
- [29] H. Lu, Y. Li, L. Zhang, and S. Serikawa. Contrast enhancement for images in turbid water. *JOSA A*, 32(5):886–893, 2015.
- [30] L. T. Maloney and B. A. Wandell. Color constancy: a method for recovering surface spectral reflectance. *JOSA A*, 3(1):29–33, 1986.
- [31] Z. Murez, T. Treibitz, R. Ramamoorthi, and D. Kriegman. Photometric stereo in a scattering medium. In *Proc. IEEE ICCV*, pages 3415–3423, 2015.
- [32] S. G. Narasimhan, M. Gupta, C. Donner, R. Ramamoorthi, S. K. Nayar, and H. W. Jensen. Acquiring scattering properties of participating media by dilution. *ACM Trans. on Graphics (TOG)*, 25(3):1003–1012, 2006.
- [33] K. Nishino, L. Kratz, and S. Lombardi. Bayesian defogging. *IJCV*, 98(3):263–278, 2012.
- [34] D. Nourisson, F. Scapini, L. Massi, and L. Lazzara. Characterisation of a tunisian coastal lagoon through hyperspectral underwater irradiance. *African J. of Aquatic Science*, 41(2):217–225, 2016.
- [35] J.-I. Park, M.-H. Lee, M. D. Grossberg, and S. K. Nayar. Multispectral imaging using multiplexed illumination. In *Proc. IEEE ICCV*, 2007.
- [36] K.-E. Peiponen, R. Myllylä, and A. V. Priezzhev. *Optical measurement techniques: innovations for industry and the life sciences*, volume 136. Springer, 2009.

- [37] A. Reinart, A. Herlevi, H. Arst, and L. Sipelgas. Preliminary optical classification of lakes and coastal waters in estonia and south finland. *J. of Sea Research*, 49(4):357–366, 2003.
- [38] F. Romeiro and T. Zickler. Blind reflectometry. In *Proc. ECCV*, pages 45–58, 2010.
- [39] Y. Y. Schechner and N. Karpel. Clear underwater vision. In *Proc. IEEE CVPR*, 2004.
- [40] Y. Y. Schechner and N. Karpel. Recovery of underwater visibility and structure by polarization analysis. *IEEE J. Oceanic Engineering*, 30(3):570–587, 2005.
- [41] Y. Y. Schechner, S. G. Narasimhan, and S. K. Nayar. Instant dehazing of images using polarization. In *Proc. IEEE CVPR*, 2001.
- [42] D. Slater and G. Healey. What is the spectral dimensionality of illumination functions in outdoor scenes? In *Proc. IEEE CVPR*, pages 105–110. IEEE, 1998.
- [43] M. G. Solonenko and C. D. Mobley. Inherent optical properties of jerlov water types. *Applied optics*, 54(17):5392–5401, 2015.
- [44] O. Spier, T. Treibitz, and G. Gilboa. *In Situ* target-less calibration of turbid media. In *Proc. IEEE ICCP*, 2017.
- [45] A. Stockman and L. T. Sharpe. The spectral sensitivities of the middle-and long-wavelength-sensitive cones derived from measurements in observers of known genotype. *Vision research*, 40(13):1711–1737, 2000.
- [46] L. D. Talley. *Descriptive physical oceanography: an introduction*. Academic press, 2011.
- [47] R. Tan. Visibility in bad weather from a single image. In *Proc. IEEE CVPR*, 2008.
- [48] T. Treibitz and Y. Y. Schechner. Active polarization descattering. *IEEE Trans. PAMI*, 31(3):385–399, 2009.
- [49] K. J. Waters, R. C. Smith, and M. R. Lewis. Avoiding ship-induced light-field perturbation in the determination of oceanic optical properties. *Oceanography*, 3(2):18–21, 1990.
- [50] P. J. Werdell, S. Bailey, G. Fargion, C. Pietras, K. Knobelspiesse, G. Feldman, and C. McClain. Unique data repository facilitates ocean color satellite validation. *Eos, Transactions American Geophysical Union*, 84(38):377–387, 2003.
- [51] G. Winters, R. Holzman, A. Blekhman, S. Beer, and Y. Loya. Photographic assessment of coral chlorophyll contents: implications for ecophysiological studies and coral monitoring. *J. Exp. Marine Biology and Ecology*, 380(1):25–35, 2009.
- [52] A. Yamashita, M. Fujii, and T. Kaneko. Color registration of underwater images for underwater sensing with consideration of light attenuation. In *IEEE. Conf. Robotics and Automation*, pages 4570–4575, 2007.